Blood Flow Velocity Field Estimation Via Spatial Regression With PDE Penalization

Laura Azzimonti, Laura M. Sangalli, Piercesare Secchi, Maurizio Domanin & Fabio Nobile

Blood Flow Velocity Field Estimation Via Spatial Regression With PDE Penalization

Laura AZZIMONTI, Laura M. SANGALLI, Piercesare SECCHI, Maurizio DOMANIN, and Fabio NOBILE

We propose an innovative method for the accurate estimation of surfaces and spatial fields when prior knowledge of the phenomenon under study is available. The prior knowledge included in the model derives from physics, physiology, or mechanics of the problem at hand, and is formalized in terms of a partial differential equation governing the phenomenon behavior, as well as conditions that the phenomenon has to satisfy at the boundary of the problem domain. The proposed models exploit advanced scientific computing techniques and specifically make use of the finite element method. The estimators have a penalized regression form and the usual inferential tools are derived. Both the pointwise and the areal data frameworks are considered. The driving application concerns the estimation of the blood flow velocity field in a section of a carotid artery, using data provided by echo-color Doppler. This applied problem arises within a research project that aims at studying atherosclerosis pathogenesis. Supplementary materials for this article are available online.

KEY WORDS: Finite elements; Functional data analysis; Object-oriented data analysis; Penalized regression; Spatial data analysis.

1. INTRODUCTION

In this work, we propose a nonparametric regression technique for surface and spatial field estimation, able to include prior knowledge on the shape of the surface or spatial field and to comply with complex conditions at the boundary of the problem domain. The motivating applied problem concerns the estimation of the blood flow velocity field on a cross-section of an artery, using data provided by echo-color Doppler (ECD) acquisitions. This study is carried out within the project *MAthematics for CARotid ENdarterectomy @ MOX* (the *MACAREN@MOX* project involves Ca' Granda Ospedale Maggiore Policlinico – Milano, the MOX Laboratory for Modeling and Scientific Computing - Dipartimento di Matematica - Politecnico di Milano, the Dipartimento di Ingegneria – Università degli studi di Bergamo, and the Mathematics Institute of Computational Science and Engineering – École Polytechnique Fédérale de Lausanne.), which gathers researchers in statistics, numerical analysis, and computer sciences and medical doctors in cardiac surgery, with the aim of investigating the pathogenesis of atherosclerosis in human carotids. The project intends specifically to study the role of blood fluid dynamics and vessel morphology on the formation process and histological properties

of atherosclerotic plaques. Interactions between the hemodynamics and atherosclerotic plaques have been highlighted for instance in Moyle, Antiga, and Steinman ([2006]) via numerical simulations of the blood flow on real patient-specific vessel morphologies.

The data collected within the project include: ECD measurements of blood flow at a cross-section of the common carotid artery, 2 cm before the carotid bifurcation, for patients affected by high-grade stenosis (>70%) in the internal carotid artery; the reconstruction of the shape of this cross-section obtained via segmentation of magnetic resonance imaging (MRI) data. The first phase of the project requires the estimation, starting from these data, of the blood flow velocity fields in the considered carotid section. These estimates are first of all of interest to the medical doctors, as they highlight relevant features of the blood flow, such as the eccentricity and the asymmetry of the flow or the reversion of the fluxes, which could have an impact on the pathology. Moreover, they will enable a population study that explores quantitatively the relationship between the blood flow and the atherosclerosis. Finally, the estimated blood velocity fields will also be used as patient-specific and physiological inflow conditions for hemodynamics simulations, which in turns aim at further enhancing the knowledge on this relationship. Analogous problems in hemodynamics were described in D'Elia, Perego, and Veneziani ([2012]), D'Elia and Veneziani ([2012]), and in Rozza, Manzoni, and Negri ([2012]).

Carotid ECD is a medical imaging procedure that uses reflected ultrasound waves to create images of an artery and to measure the velocity of blood cells in some locations within the artery. This technique does not require the use of contrast media or ionizing radiation and has relative low cost. Thanks to this complete noninvasivity and also to the short acquisition time required, ECD scans are largely used in clinics, even though they provide a less rich and noisier information than other diagnostic devices, such as phase contrast magnetic resonance imaging. Figure 1, left panel, shows one of the ECD images used in the study. The ultrasound image in the upper part of the
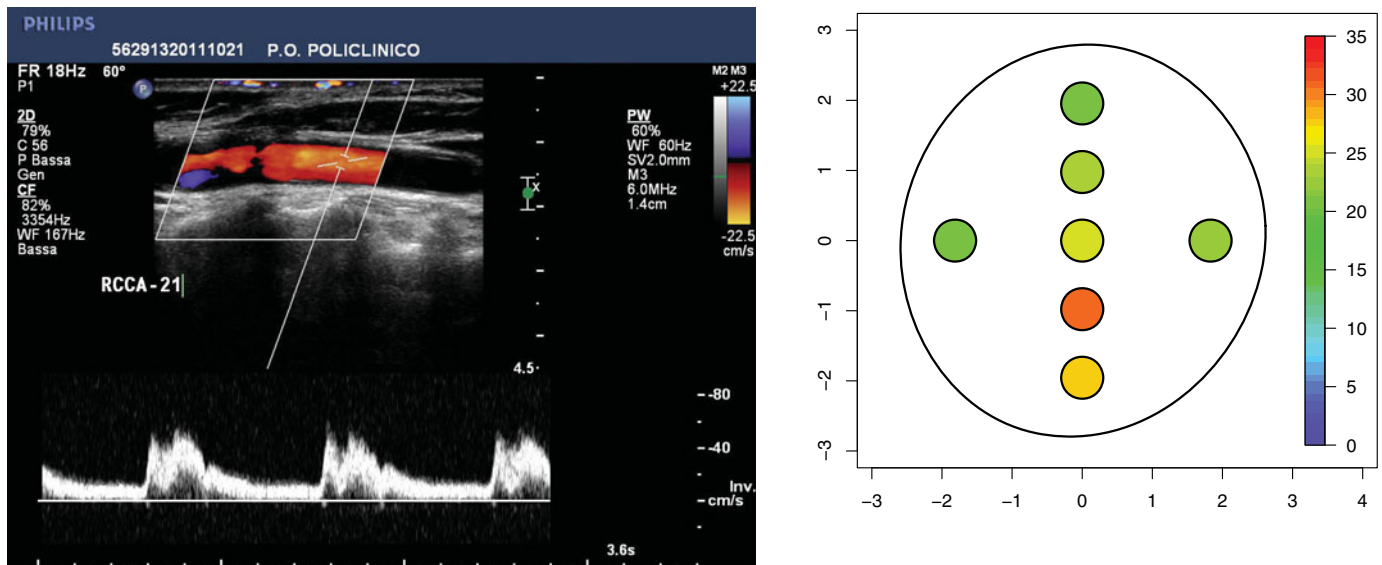
Figure 1. Left panel: ECD image corresponding to the central point of the carotid section located 2 cm before the carotid bifurcation. Right panel: MRI reconstruction of the cross-section of the carotid artery located 2 cm before the carotid bifurcation; cross-shaped pattern of observations with each beam colored according to the mean blood velocity measured (c/ms) on the beam at systolic peak time.

figure represents the longitudinal section of the vessel. It also shows by a small gray box the position of the beam where blood particle velocities, in the longitudinal direction of the vessel, are measured; the dimension of the box relates to the dimension of the beam. In the case considered in this picture, the acquisition beam is located in the center of the considered cross-section of the artery. The lower part of the ECD image is a graphical display of the acquired velocity signal during the time lapse of about three heart-beats. This signal represents the histogram of the measured velocities, evolving in time. More precisely, the *x*-axis represents time and the *y*-axis represents velocity classes; for any fixed time, the gray-scaled intensity of pixels is proportional to the number of blood cells in the beam moving at a certain velocity. For the purpose of this work, we shall consider a fixed time instant corresponding to the systolic peak, which is of crucial clinical interest.

Figure 1, right panel, shows the reconstruction from MRI data of the considered cross-section of the carotid artery; it also displays the spatial locations of the beams inspected in the ECD scan. In particular, during the ECD scan seven beams are considered, located in a cross-shaped pattern; this unusual pattern is a compromise decided together with clinicians to obtain as many observations as possible in the short time dedicated to the acquisition. In the figure, each beam is colored according to the value of the mean velocity registered within the beam at the fixed time instant considered, the systolic peak.

In this applied problem, there are important conditions at the boundary of the problem domain, that is, specifically, at the wall of the carotid cross-section represented in Figure 1, right panel. The physics of the problem implies in fact that blood flow velocity is zero at the arterial wall, due to the friction between blood cells and arterial wall; these are the so-called no-slip boundary conditions.

Classical methods for surface estimation, as tensor product of unidimensional splines, thin-plate splines, bidimensional kernel smoothing, bidimensional wavelet-based smoothing, and krig-

ing, are naturally defined on tensorized domains and do not efficiently deal with more complex domains, when the shape of the domain is important for the behavior of the phenomenon under study. Moreover, they cannot naturally include information on the value of the surface at the boundary, although it is possible to enforce such boundary conditions, for example, with binning. Recently, some methods have been proposed where the shape of the domain and the boundary conditions are instead directly specified in the model. For instance, finite element L-splines described in Ramsay (2002) account explicitly for the shape of the domain, efficiently dealing with irregular-shaped domains; soap-film smoothing (SOAP), described in Wood, Bravington, and Hedley (2008), considers both the shape of the domain and some common types of boundary conditions; spatial spline regression (SSR), presented in Sangalli, Ramsay, and Ramsay (2013), extends Ramsay (2002) and includes general boundary conditions. The methods in Ramsay (2002), Wood, Bravington, and Hedley (2008) and Sangalli, Ramsay, and Ramsay (2013) are penalized regression methods with a roughness term involving the Laplacian of the field, the Laplacian being a simple form of partial differential operator that provides a measure of the local curvature of the field. Although being able to account for the shape of the domain and to comply with the required boundary conditions, these methods do not provide physiological estimates of the blood flow velocity field. Figure 2 shows, for example, the velocity field estimated using SSR. The penalization of a measure of the local curvature of the field oversmooths and flattens the field toward a plane in those regions of the domain where no observations are available; the resulting estimated velocity field has thus rhomboidal isolines, which are certainly nonphysiological.

On the other hand, we have prior knowledge on the phenomenon under study that could be exploited to derive accurate physiological estimates. There is in fact a vast literature devoted to the study of fluid dynamics and hemodynamics, see,
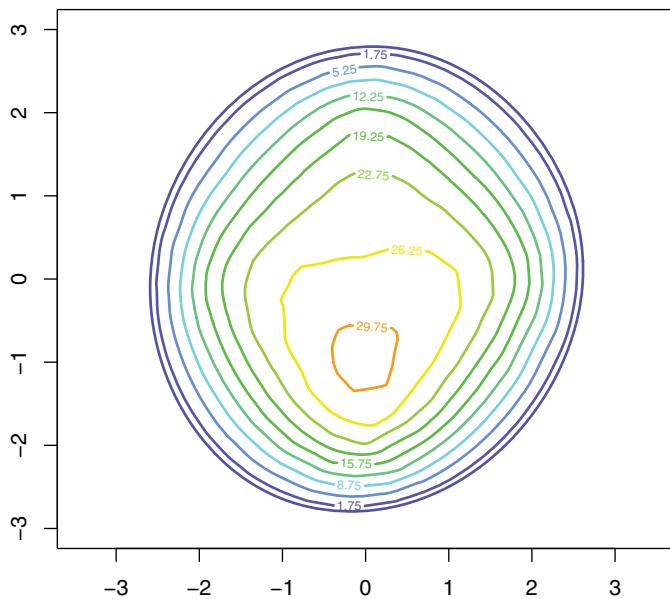
Figure 2. Estimate of the blood flow velocity field on the carotid section using standard SSR.

for example, Formaggia, Quarteroni, and Veneziani (2009), and references therein. For what serves our purpose, it suffices to know that the theoretical solution of a stationary velocity field in a straight pipe with circular section has a parabolic profile. In our application, during the systolic phase, we hence expect to obtain a velocity field similar in shape to a parabolic profile, with smooth isolines resembling circles. Notice that the real blood velocity field is not perfectly parabolic due to the curvature of the artery, the nonstationarity of the blood flow and the imperfect circularity of the artery section. For instance, the curvature of the artery and the nonstationarity in time of the blood flow may induce asymmetries and eccentricities in the blood flow. For this reason, imposing a parametric model that forces the estimate to be a parabolic profile with circular isolines would not be appropriate; such a model would, for instance, completely miss the physiological asymmetries and eccentricities of the flow. Nevertheless, this prior information concerning the shape of the field, which can be conveniently translated into a partial differential operator, could be incorporated in a nonparametric model, along with the desired boundary conditions. Partial differential equations (PDEs) are a multidimensional extension of ordinary differential equations (ODEs); their study though requires different and more complex analytical and numerical techniques with respect to those used for ODEs; see, for example, Evans (1998).

In this work, extending Ramsay (2002) and Sangalli, Ramsay, and Ramsay (2013), we propose a nonparametric model that includes prior information on the phenomenon under study, coming for instance from the physics, physiology, mechanics, or chemistry of the problem, and formalized in terms of a governing PDE. Specifically, spatial regression with PDE penalization (SR-PDE) features a roughness term that involves, instead of the simple Laplacian, a more general PDE modeling of the phenomenon. The applicability of the proposed method is by no way restricted to the problem here considered; PDEs are in fact commonly used to describe complex phenomena be-

havior in many fields of engineering and sciences, including bio-sciences, geo-sciences, and physical sciences. Applications of particular interest in the environmental sciences concern, for example, the study of the dispersion of pollutant released in water or in air and transported by streams or winds, the study of temperature, pressure and electromagnetic fields, the study of the propagation of earthquakes, tsunamis, and other wave phenomena. Important applications in biomedicine include also the study of electrophysiology and mechanics of organs and the study of tumor growth dynamics. It should be noted that many methods for surface and spatial field estimation, besides the already cited SSR and SOAP, use roughness penalties involving some simple form of PDEs. A classical example is given by thin-plate-splines, while a recent proposal was offered, for instance, by Guillas and Lai (2010). Our work has also strong connections with the framework introduced by Lindgren, Rue, and Lindström (2011), and more generally with the larger literature on Bayesian inverse problem, see, for example, Stuart (2010). In particular, Lindgren, Rue, and Lindström (2011) proposed Bayesian spatial models that link Gaussian fields and Gaussian Markov random fields via a stochastic PDE inducing a Matérn covariance. One important novelty of the proposed SR-PDE models with respect to the methods cited above is that the PDE is here used to model the space variation of the phenomenon, using problem-specific information. Moreover, SR-PDE allows for important modeling flexibility in this respect, accounting also for space anisotropy and nonstationarity in a straightforward way, as well as unidirectional smoothing effects. The approach used to solve the surface estimation problem borrows techniques from PDEs control theory, see, for example, Hinze et al. (2009), and Lions (1971) and Quarteroni (2008). However, the viewpoint that we have in this work is quite different from the classical control theory framework, where the main interest is focused on surface estimation starting from integral targets, usually known without error, instead of partial, pointwise, and noisy observations. For this reason, different questions have to be addressed in our framework, with respect to those classically considered in control theory. Finally, the smoothing method here proposed could in principle be further extended also to a larger class of penalty terms, including higher-order operators or nonlinear operators, provided that the associated differential problems are well posed. However, their numerical approximation may become much more involved.

Likewise in Ramsay (2002) and Sangalli, Ramsay, and Ramsay (2013), SR-PDE exploits advanced numerical analysis techniques and, specifically, it makes use of the finite element method, which provides a basis for piecewise polynomial surfaces. The resulting estimators have a penalized regression form, they are linear in the observed data values and classical inferential tools can be derived. The proposed method is currently implemented in R, see R Development Core Team (2012), and in FreeFem++, see Pironneau et al. (2011).

The article is organized as follows. Section 2 introduces SR-PDE for pointwise observations. Section 3 extends the models to the case of areal data, which is of interest in many applications, including the analysis of ECD measurements here considered. Section 4 describes the finite element solution to the estimation problem and derives the inferential properties of the estimators. Section 5 deals with general boundary conditions. In Section 6,

SR-PDE is compared to standard SSR and to SOAP in different simulation settings, with data distributed uniformly on the domain or only on some subregions, showing that the inclusion of the prior knowledge on the phenomenon behavior improves significantly the estimates. In Section 7, the application within the MACAREN@MOX project is presented: details on the ECD acquisitions are given and the results obtained with SR-PDE are shown. Section 8 outlines future research directions.

2. MODEL FOR POINTWISE DATA

Consider a bounded and regular domain $\Omega \subset \mathbb{R}^2$, whose boundary $\partial\Omega$ is a curve of class C^2, and n observations z_i, for $i = 1, \ldots, n$, located at points $\mathbf{p}_i = (x_i, y_i) \in \Omega$. Assume the model

$$z_i = f_0(\mathbf{p}_i) + \epsilon_i, \tag{1}$$

where ϵ_i, $i = 1, \ldots, n$, are independent errors with zero mean and constant variance σ^2, and $f_0 : \Omega \to \mathbb{R}$ is the surface or spatial field to be estimated. In our application, Ω will be the carotid cross-section of interest, the observations z_i will represent the blood particles' velocities measured by ECD in the longitudinal direction of the artery (i.e., in the orthogonal direction to Ω) and the surface f_0 will represent the longitudinal velocity field on the carotid cross-section.

Assume that problem-specific prior information is available, which can be described in terms of a PDE, $Lf_0 = u$, modeling to some extent the phenomenon under study; moreover, prior knowledge could also concern possible conditions that f_0 has to satisfy at the boundary $\partial\Omega$ of the problem domain. Generalizing the models in Ramsay (2002) and Sangalli, Ramsay, and Ramsay (2013), we propose to estimate f_0 by minimizing the penalized sum-of-square-error functional

$$J(f) = \sum_{i=1}^{n} (f(\mathbf{p}_i) - z_i)^2 + \lambda \int_{\Omega} \left(Lf(\mathbf{p}) - u(\mathbf{p})\right)^2 d\mathbf{p} \tag{2}$$

with respect to $f \in V$, where V is the space of functions in $L^2(\Omega)$ with first and second derivatives in $L^2(\Omega)$ that satisfy the required boundary conditions (b.c.). The penalized error functional hence trades off a data-fitting criterion, the sum-of-square-error, and a model-fitting criterion, which penalizes departures from a PDE problem-specific description of the phenomenon. Because of the inclusion of a PDE in the definition of the statistical model, the proposed method can be seen as a regularized least square analogous to the Bayesian inverse problems presented, for example, in Stuart (2010). In particular, the least square term in $J(f)$ corresponds to a log-likelihood for Gaussian errors, while the regularizing term effectively translates the prior knowledge on the surface. With respect to Stuart (2010), besides the different model framework and estimation approaches, we also deal with a larger class of operators, including nonstationary anisotropic diffusion, transport, and reaction terms.

In particular, we consider here phenomena that are well described in terms of linear second-order elliptic operators L and forcing term $u \in L^2(\Omega)$ that can be either $u = 0$, homogenous case, or $u \neq 0$, nonhomogenous case. The operator L is a general differential operator that can, for instance, include second-, first-, and zero-order differential operators. Consider a symmetric and

positive definite matrix $\mathbf{K} = \{K_{ij}\}_{i,j=1,2} \in \mathbb{R}^{2\times2}$, named diffusion tensor, a vector $\mathbf{b} = (b_1, b_2) \in \mathbb{R}^2$, named transport vector, and a positive scalar $c \in \mathbb{R}^+$, named reaction term. Then, the operator can include: second-order differential operators as the divergence of the gradient, that is,

$$\text{div}(\mathbf{K}\nabla f) = \frac{\partial}{\partial x}\left(K_{11}\frac{\partial f}{\partial x} + K_{12}\frac{\partial f}{\partial y}\right)$$
$$+ \frac{\partial}{\partial y}\left(K_{21}\frac{\partial f}{\partial x} + K_{22}\frac{\partial f}{\partial y}\right),$$

first-order differential operators as the gradient, that is,

$$\mathbf{b} \cdot \nabla f = b_1\frac{\partial f}{\partial x} + b_2\frac{\partial f}{\partial y},$$

and also zero-order operators, that is, cf. The general form that we consider is

$$Lf = -\text{div}(\mathbf{K}\nabla f) + \mathbf{b} \cdot \nabla f + cf. \tag{3}$$

The three terms that compose the general second-order operator (3) induce an anisotropic and nonstationary smoothing, providing different regularizing effects. The diffusion term $-\text{div}(\mathbf{K}\nabla f)$ induces a smoothing in all the directions; if the diffusion matrix $\mathbf{K}$ is a multiple of the identity, the diffusion term has an isotropic smoothing effect, otherwise it implies an anisotropic smoothing with a preferential direction that corresponds to the first eigenvector of the diffusion tensor $\mathbf{K}$. The degree of anisotropy induced by the diffusion tensor $\mathbf{K}$ is controlled by the ratio between its first and second eigenvalue. It is possible to visualize the diffusion term as the quadratic form in $\mathbb{R}^2$ induced by the tensor $\mathbf{K}^{-1}$. On the contrary, the transport term $\mathbf{b} \cdot \nabla f$ induces a smoothing only in the direction specified by the transport vector $\mathbf{b}$. Finally, the reaction term cf has instead a shrinkage effect, since penalization of the L^2 norm of f induces a shrinkage of the surface to zero. Setting $\mathbf{K} = \mathbf{I}$, $\mathbf{b} = \mathbf{0}$, $c = 0$, and $u = 0$, we obtain the special case described in Ramsay (2002) and Sangalli et al. (2013), where the penalization of the Laplacian Δf induces an isotropic and stationary smoothing.

The parameters of the differential operator L can also be space-varying on Ω; that is, $\mathbf{K} = \mathbf{K}(x, y)$, $\mathbf{b} = \mathbf{b}(x, y)$, and $c = c(x, y)$. This feature is fundamental to translate the a priori information on the phenomenon. For instance, in the blood flow velocity application, the problem-specific prior information can be described via an appropriate anisotropic and nonstationary differential operator that includes: a nonstationary anisotropic diffusion tensor that smooths the observations in the tangential direction of concentric circles (see Figure 3, center); a nonstationary transport field that smooths the observations in the radial direction, from the center of the section to the boundary (see Figure 3, right). The reaction term is instead not required in this application. The nonstationary and anisotropic diffusion tensor field $\mathbf{K}$ used in the application and represented in the central panel of Figure 3 can be compared to the stationary and isotropic diffusion tensor field $\mathbf{K} = \mathbf{I}$ used in SSR and represented in the left panel of Figure 3. Notice that the space-varying parameters need to satisfy some regularity conditions to ensure that the solution of the corresponding PDE is regular enough for the estimation problem to be well posed (see Section 1 in the supplementary material available online). The functional $J(f)$
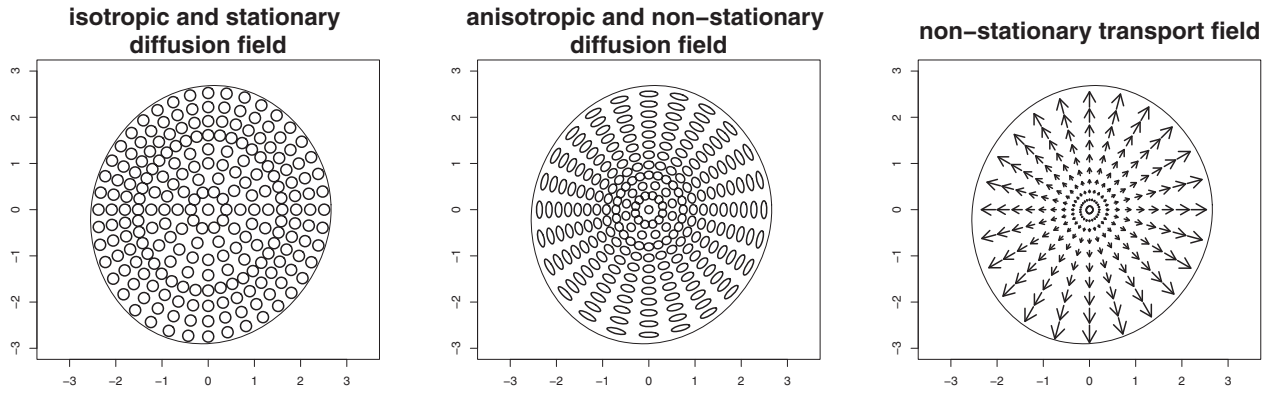
Figure 3. Left: stationary and isotropic diffusion tensor $\mathbf{K} = \mathbf{I}$ used in the blood flow velocity field application for SSR. Center and right: nonstationary and anisotropic diffusion tensor field $\mathbf{K}$ and nonstationary transport field $\mathbf{b}$, used in the blood flow velocity field application for SR-PDE: the displayed tensor field $\mathbf{K}$ smooths the observations in the tangential direction of concentric circles, while the transport field $\mathbf{b}$ smooths the observations in the radial direction, from the center of the carotid section to the arterial wall.

is well defined if $f \in V$ since $V \subset C(\bar{\Omega})$ if $\Omega \subset \mathbb{R}^2$ and the misfit of the PDE is square integrable.

We can impose different types of boundary conditions, homogenous or not, that involve the evaluation of the function and/or its first derivative at the boundary, allowing for a complex modeling of the behavior of the surface at the boundary $\partial\Omega$ of the domain. For ease of notation, we consider in the following the simple case of homogenous Dirichlet b.c., which involves the value of the function at the boundary, clamping it to zero, that is, $f|_{\partial\Omega} = 0$. These boundary conditions correspond to the physiological no-slip conditions needed in the ECD application; the blood cells have in fact zero longitudinal velocity near the arterial wall due to friction between the blood particles and the arterial wall. In Section 2 of the supplementary material available online, we extend all the results presented in this section to the case of more general nonhomogenous boundary conditions that can also involve first derivatives. In this work, the boundary conditions are directly included in the space V; in the case of Dirichlet homogenous b.c., V is the space of functions in $L^2(\Omega)$ with first and second derivatives in $L^2(\Omega)$ and zero value at the boundary $\partial\Omega$.

To lighten the notation, surface integrals will be written without the integration variable $\mathbf{p}$; unless differently specified, the integrals are computed with respect of the Lebesgue measure, that is, $\int_D q = \int_D q(\mathbf{p})d\mathbf{p}$, for any $D \subseteq \mathbb{R}^2$ and integrable function q.

All the results presented can also be extended to include space-varying covariate information, following the semiparametric approach described in Sangalli, Ramsay, and Ramsay (2013).

2.1 Solution to The Estimation Problem

The estimation problem can be formulated as follows.

Problem 1. Find $\hat{f} \in V$ such that

$$\hat{f} = \operatorname*{argmin}_{f \in V} J(f).$$

Proposition 1. Under suitable regularity conditions for L, the solution of Problem 1 exists and is unique.

The required regularity conditions, the proof of Proposition 1, and the solution of the estimation problem are detailed in Section 1 of the supplementary material available online. The key idea consists in exploiting the linearity of the PDE penalized in the roughness term to prove the convexity of the functional $J(f)$. The minimum is then obtained by differentiating the functional $J(f)$ with respect to f. The differentiation of the functional $J(f)$ provides an explicit expression for the surface estimate $\hat{f}$ as the solution of a linear fourth-order problem. A convenient way to solve this fourth-order problem is to split it into the following coupled system of second-order PDEs:

$$\begin{cases} L\hat{f} = u + \hat{g} & \text{in } \Omega \\ \hat{f} = 0 & \text{on } \partial\Omega \end{cases} \quad \begin{cases} L^*\hat{g} = -\frac{1}{\lambda}\sum_{i=1}^n(\hat{f} - z_i)\delta_{\mathbf{p}_i} & \text{in } \Omega \\ \hat{g} = 0 & \text{on } \partial\Omega \end{cases},$$
(4)

where $\hat{g}$ represents the misfit of the penalized PDE, that is, $\hat{g} = L\hat{f} - u$, L^* is the adjoint operator of L, that is, is such that $\int_\Omega L\varphi\psi = \int_\Omega \varphi L^*\psi$ for all $\varphi, \psi \in V$, and is defined as

$$L^*\hat{g} = -\operatorname{div}(\mathbf{K}\nabla\hat{g}) - \mathbf{b} \cdot \nabla\hat{g} + (c - \operatorname{div}(\mathbf{b}))\hat{g}. \quad (5)$$

The coupled system of PDEs (4) is then solved by means of the finite element method, which is a standard technique used to solve PDEs (see, e.g., Quarteroni 2008), to obtain a piecewise polynomial discretization of the surface estimate.

3. MODEL FOR AREAL DATA

We here extend the surface smoothing method presented in the previous section to the case of areal data, a setting common in many applications, including the one driving our study.

Let $D_i \subset \Omega$, for $i = 1, \ldots, N$, be some subdomains where we have observations and z_{ij}, for $j = 1, \ldots, n_i$, be the observations located at point $\mathbf{p}_{ij} \in D_i$. For the observations z_{ij}, we consider the pointwise model (1), that is,

$$z_{ij} = f_0(\mathbf{p}_{ij}) + \epsilon_{ij}, \quad (6)$$

where ϵ_{ij}, for $i = 1, \ldots, N$ and $j = 1, \ldots, n_i$, are independent errors with zero mean and constant variance σ^2.

In the blood flow velocity application, the location points $\mathbf{p}_{ij}$ are unknown, the only available information being that $\mathbf{p}_{ij} \in D_i$, where D_i is the ith ECD acquisition beam. We may assume that the location points $\mathbf{p}_{ij}$ are distributed over the subdomains

according to a global uniform distribution over Ω and that the subdomains are not overlapping. For each beam D_i, the ECD signal (Figure 1, left panel) provides, at a fixed time, a histogram of the measured blood particle velocities. We summarize the information carried by the histogram by its mean value. Specifically, let $\bar{z}_i$ be the mean value of the observations on the subdomain D_i, for $i = 1, \ldots, N$. From (6), we can derive the following model for this variable:

$$\bar{z}_i = \frac{1}{n_i} \sum_{j=1}^{n_i} f_0(\mathbf{p}_{ij}) + \frac{1}{n_i} \sum_{j=1}^{n_i} \epsilon_{ij},$$

where $\sum_{j=1}^{n_i} \epsilon_{ij}/n_i$, $i = 1, \ldots, N$, are errors with zero mean and variance σ^2/n_i.

The quantity $\sum_{j=1}^{n_i} f_0(\mathbf{p}_{ij})/n_i$ is the Monte Carlo approximation of $\mathbb{E}\left[f_0(P) \mid P \in D_i \right]$ and the latter is in turn equal to the spatial average of the surface on the subdomain D_i, under the assumption of uniformly distributed observation points, that is,

$$\frac{1}{n_i} \sum_{j=1}^{n_i} f_0(\mathbf{p}_{ij}) \approx \mathbb{E}\left[f_0(P) \mid P \in D_i \right] = \frac{1}{|D_i|} \int_{D_i} f_0.$$

We may thus consider the following model:

$$\bar{z}_i = \frac{1}{|D_i|} \int_{D_i} f_0 + \eta_i, \tag{7}$$

where the error terms η_i have zero mean and variances $\bar{\sigma}_i^2$ inversely proportional to the dimension of the beams D_i; this assumption on the variances is coherent with the assumption on location points being distributed on the subdomains according to a uniform distribution (so that in fact the average number of observations on each subdomain is proportional to the dimension of the subdomain). If the subdomains have the same dimension, as it is in fact the case in our application, this simplifies to variances all equal to $\bar{\sigma}^2$.

To estimate the surface, we hence propose to minimize the penalized sum-of-square-error functional

$$\bar{J}(f) = \sum_{i=1}^{N} \frac{1}{|D_i|} \left(\int_{D_i} (f - \bar{z}_i) \right)^2 + \lambda \int_{\Omega} (Lf - u)^2 \tag{8}$$

with respect to $f \in V$. The first term is now a weighted least-square-error functional for areal data on the subdomains D_i, where the weights are in fact equal to the inverse of the variances $\bar{\sigma}_i^2$, being $\bar{\sigma}_i^2 \propto 1/|D_i|$. Notice that the functional (8) mixes two different kinds of information: the data provide information only on the areal means of the surface f over the subdomains, while the roughness penalty translates the prior knowledge directly on the shape of f.

3.1 Solution to The Estimation Problem

The estimation problem can be formulated as follows.

Problem 2. Find $\hat{f} \in V$ such that

$$\hat{f} = \underset{f \in V}{\operatorname{argmin}} \, \bar{J}(f).$$

Proposition 2. Under suitable regularity conditions for L, the solution of Problem 2 exists and is unique.

Details on the regularity conditions and on the proof are provided in Section 1 of the supplementary material available online. The proof follows the same strategy used in the proof of Proposition 1. Moreover, using the same arguments as for the pointwise case it can be shown that the surface estimator $\hat{f}$ can be obtained by solving a fourth-order problem and that the latter problem can be conveniently split into the following coupled system of second-order problems:

$$\begin{cases} L\hat{f} = u + \hat{g} & \text{in } \Omega \\ \hat{f} = 0 & \text{on } \partial\Omega \\ L^*\hat{g} = -\frac{1}{\lambda} \sum_{i=1}^{N} \frac{1}{|D_i|} \mathbb{I}_{D_i} \int_{D_i} (\hat{f} - \bar{z}_i) & \text{in } \Omega \\ \hat{g} = 0 & \text{on } \partial\Omega, \end{cases} \tag{9}$$

where $\hat{g}$ represents the misfit of the PDE penalized, that is, $\hat{g} = L\hat{f} - u$, and L^* is the adjoint operator of L, defined in (5). As in the pointwise case, the coupled system of PDEs (9) is then discretized by means of the finite element method.

Remark 1. All the results presented in this section can be extended to the case of location points distributed on the subdomains according to a general known global distribution μ over Ω, $P \sim \mu$. The quantity $\sum_{j=1}^{n_i} f_0(\mathbf{p}_{ij})/n_i$ is in fact, also in this case, the Monte Carlo approximation of $\mathbb{E}\left[f_0(P) \mid P \in D_i \right]$:

$$\frac{1}{n_i} \sum_{j=1}^{n_i} f_0(\mathbf{p}_{ij}) \approx \mathbb{E}\left[f_0(P) \mid P \in D_i \right] = \frac{1}{\mu(D_i)} \int_{D_i} f_0(\mathbf{p})\mu(d\mathbf{p}).$$

Therefore, the model for the areal mean on the subdomains becomes

$$\bar{z}_i = \frac{1}{\mu(D_i)} \int_{D_i} f_0(\mathbf{p})\mu(d\mathbf{p}) + \eta_i.$$

Under the assumption of nonoverlapping subdomains, the errors η_i have zero mean and variances inversely proportional to $\mu(D_i)$, which is the probability of sampling a point in the subdomain D_i. The surface estimator $\hat{f}$ can be obtained minimizing the weighted least-square functional

$$\bar{J}_\mu(f) = \sum_{i=1}^{N} \frac{1}{\mu(D_i)} \left(\int_{D_i} (f(\mathbf{p}) - \bar{z}_i)\,\mu(d\mathbf{p}) \right)^2 + \lambda \int_{\Omega} (Lf - u)^2$$

with respect to $f \in V$. The weights in the least square term are proportional to the inverse of $\text{var}(\bar{z}_i)$, being $\text{var}(\bar{z}_i) \propto 1/\mu(D_i)$.

4. FINITE ELEMENT SOLUTION TO THE ESTIMATION PROBLEM

The surface estimation problems in the pointwise and areal data frameworks presented, respectively, in Sections 2 and 3 are infinite-dimensional problems and cannot be solved analytically. A standard approach to handle these problems is to reformulate them in a proper finite-dimensional subspace that approximates the original infinite-dimensional one. This approach is used in many fields of statistics and applied mathematics, for example, nonparametric statistics, functional and spatial data analysis, and analysis of differential equations. In particular, the standard method used in numerical analysis to solve PDEs is the finite element method (see, e.g., Quarteroni 2008), which provides a basis for continuous piecewise polynomial surfaces over a triangulation of the domain of interest. The discretization of a surface by means of finite elements is similar to the discretization of a

curve by means of univariate splines, the latter providing a basis for piecewise polynomial curves.

Let $\mathcal{T}_h$ be a triangulation of the domain, where h denotes the characteristic mesh size, defined as the maximum length of the triangle edges in the triangulation. Figure 4, left panel, shows the triangulation considered in the velocity field application. We consider the space V_h^r of piecewise polynomial functions of order $r \geq 1$ over the triangulation. Denoting with $\mathbb{P}^r(\boldsymbol{\tau})$ the space of polynomial functions of order r over the triangle $\boldsymbol{\tau}$, the space V_h^r is defined as

$$V_h^r = \left\{ v \in C^0(\bar{\Omega}) : v|_{\boldsymbol{\tau}} \in \mathbb{P}^r(\boldsymbol{\tau}) \ \forall \boldsymbol{\tau} \in \mathcal{T}_h \right\}. \quad (10)$$

The space V_h^r is a finite-dimensional subspace of $H^1(\Omega)$, which is the space of functions in $L^2(\Omega)$ with first derivatives in $L^2(\Omega)$. The latter space is characterized by less regularity than the space V, which has both first and second derivatives in $L^2(\Omega)$. It is thus necessary to appropriately reformulate the estimation problems (4) and (9) to involve only first-order derivatives, as it will be described in Sections 4.1 and 4.2.

Let $N_h = \dim(V_h^r)$ and denote by $\psi_1, \dots, \psi_{N_h}$ the finite element basis functions such that $V_h^r = \text{span}\{\psi_1, \dots, \psi_{N_h}\}$. The basis $\psi_1, \dots, \psi_{N_h}$ are associated with the nodes $\boldsymbol{\xi}_1, \dots, \boldsymbol{\xi}_{N_h}$ that correspond to the vertices of the triangulation $\mathcal{T}_h$ if the basis is piecewise linear, and are instead a superset of the vertices when the degree of the polynomial basis is higher than one. Notice that the nodes of the mesh and the mesh itself can be defined independently of the location points $\mathbf{p}_1, \dots, \mathbf{p}_n$. Figure 4, right panel, shows, for example, a linear finite element basis function on a regular triangulation. The basis functions are local basis, with compact support, that can be seen as multidimensional extensions of univariate splines. Moreover, the basis functions $\psi_1, \dots, \psi_{N_h}$ are *Lagrangian*, meaning that $\psi_k(\xi_l) = \delta_{kl}$, where $\delta_{ij} = 1$ if $i = j$ and $\delta_{ij} = 0$ otherwise. Hence, a surface $f \in V_h^r$ is uniquely determined by its values at the nodes:

$$f(x, y) = \sum_{k=1}^{N_h} f(\xi_k) \psi_k(x, y) = \boldsymbol{\psi}(x, y)^T \mathbf{f}, \quad (11)$$

where

$$\mathbf{f} = \left(f(\boldsymbol{\xi}_1), \dots, f(\boldsymbol{\xi}_{N_h}) \right)^T \quad \text{and} \quad \boldsymbol{\psi} = \left(\psi_1, \dots, \psi_{N_h} \right)^T.$$

In the following we consider only homogenous Dirichlet b.c., for which the value of the function at the boundary is fixed to 0. In this case, we consider the finite element space $V_{h,0}^r = \left\{ v \in C^0(\bar{\Omega}) : v|_{\partial\Omega} = 0 \text{ and } v|_{\boldsymbol{\tau}} \in \mathbb{P}^r(\boldsymbol{\tau}) \ \forall \boldsymbol{\tau} \in \mathcal{T}_h \right\}$, of dimension $N_{h,0}$, which only necessitates of the basis functions associated with the internal nodes of the triangulation, while the basis functions associated with the boundary nodes can be discarded. In Section 2 of the supplementary material available online, we extend the results presented in this section to the case of more general boundary conditions.

4.1 Pointwise Estimator

The finite element surface estimator $\hat{f}_h$ is obtained recasting the estimation problem in the finite-dimensional space $V_{h,0}^r$, thus obtaining a discretized version of the coupled system of PDEs (4). As previously highlighted, the estimation problem (4) is defined in V, which is a space with both first- and second-order derivatives in $L^2(\Omega)$, while the finite element space $V_{h,0}^r$ pro-

vides a finite-dimensional subspace of $H^1(\Omega)$. For this reason, we need to reformulate the estimation problem in a form that can be properly discretized using the finite element space. This appropriate reformulation of the problem, called variational formulation, involves only first-order derivatives and is obtained integrating the differential equations against a test function and integrating by parts the second-order terms.

By introducing the test function $\psi \in V_{h,0}^r$, we can define the bilinear form $a(\cdot, \cdot)$, associated with the operator L, as

$$a(\hat{f}_h, \psi_h) = \int_\Omega \left(\mathbf{K} \nabla \hat{f}_h \cdot \nabla \psi_h + \mathbf{b} \cdot \nabla \hat{f}_h \psi_h + c \hat{f}_h \psi_h \right). \quad (12)$$

The discrete surface estimators $\hat{f}_h, \hat{g}_h \in V_{h,0}^r$ are thus obtained solving

$$\begin{cases} a(\hat{f}_h, \psi_h) - \int_\Omega \hat{g}_h \psi_h = \int_\Omega u \psi_h \\ \lambda a(\varphi_h, \hat{g}_h) + \sum_{i=1}^n \hat{f}_h(\mathbf{p}_i) \varphi_h(\mathbf{p}_i) = \sum_{i=1}^n z_i \varphi_h(\mathbf{p}_i) \end{cases} \quad (13)$$

for all $\psi_h, \varphi_h \in V_{h,0}^r$. Exploiting now the finite element representation (11) for the discrete estimators $\hat{f}_h, \hat{g}_h \in V_{h,0}^r$, we are allowed to write the estimation problem as a linear system. Define $\boldsymbol{\psi}_x = (\partial\psi_1/\partial x, \dots, \partial\psi_{N_{h,0}}/\partial x)^T$ and $\boldsymbol{\psi}_y = (\partial\psi_1/\partial y, \dots, \partial\psi_{N_{h,0}}/\partial y)^T$ and the matrices

$$\mathbf{R}(c) = \int_\Omega c\boldsymbol{\psi}\boldsymbol{\psi}^T,$$

$$\mathbf{R}_x(\mathbf{b}) = \int_\Omega b_1 \boldsymbol{\psi}\boldsymbol{\psi}_x^T, \quad \mathbf{R}_y(\mathbf{b}) = \int_\Omega b_2 \boldsymbol{\psi}\boldsymbol{\psi}_y^T,$$

$$\mathbf{R}_{xx}(\mathbf{K}) = \int_\Omega K_{11} \boldsymbol{\psi}_x\boldsymbol{\psi}_x^T, \quad \mathbf{R}_{yy}(\mathbf{K}) = \int_\Omega K_{22} \boldsymbol{\psi}_y\boldsymbol{\psi}_y^T,$$

$$\mathbf{R}_{xy}(\mathbf{K}) = \int_\Omega K_{12}(\boldsymbol{\psi}_x\boldsymbol{\psi}_y^T + \boldsymbol{\psi}_y\boldsymbol{\psi}_x^T).$$

Using this notation, the finite element matrix associated with the bilinear form $a(\cdot, \cdot)$ in (12) is given by

$$\mathbf{A}(\mathbf{K}, \mathbf{b}, c) = \mathbf{R}_{xx}(\mathbf{K}) + \mathbf{R}_{xy}(\mathbf{K}) + \mathbf{R}_{yy}(\mathbf{K}) + \mathbf{R}_x(\mathbf{b})$$
$$+ \mathbf{R}_y(\mathbf{b}) + \mathbf{R}(c). \quad (14)$$

Moreover, define the vectors $\mathbf{z} = (z_1, \dots, z_n)^T$, $\mathbf{u} = \int_\Omega u\boldsymbol{\psi}$, and the matrices

$$\mathbf{R} = \mathbf{R}(1) = \int_\Omega \boldsymbol{\psi}\boldsymbol{\psi}^T$$

and

$$\boldsymbol{\Psi} = \begin{bmatrix} \boldsymbol{\psi}^T(\mathbf{p}_1) \\ \vdots \\ \boldsymbol{\psi}^T(\mathbf{p}_n) \end{bmatrix}, \quad (15)$$

where $\boldsymbol{\Psi}$ is the matrix of basis evaluations at the n data locations $\mathbf{p}_1, \dots, \mathbf{p}_n$.

The finite element solution $\hat{f}_h$ of the discrete counterpart (13) of the estimation Problem 1 is thus given by $\hat{f}_h = \boldsymbol{\psi}^T \hat{\mathbf{f}}$, where $\hat{\mathbf{f}}$ is the solution of the linear system

$$\begin{bmatrix} \boldsymbol{\Psi}^T\boldsymbol{\Psi} & \lambda\mathbf{A}^T \\ \mathbf{A} & -\mathbf{R} \end{bmatrix} \begin{bmatrix} \hat{\mathbf{f}} \\ \hat{\mathbf{g}} \end{bmatrix} = \begin{bmatrix} \boldsymbol{\Psi}^T\mathbf{z} \\ \mathbf{u} \end{bmatrix}.$$
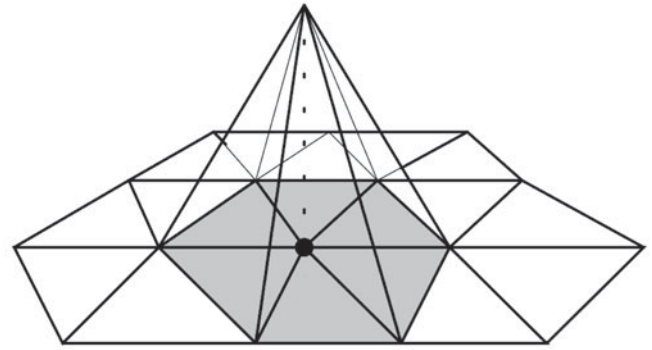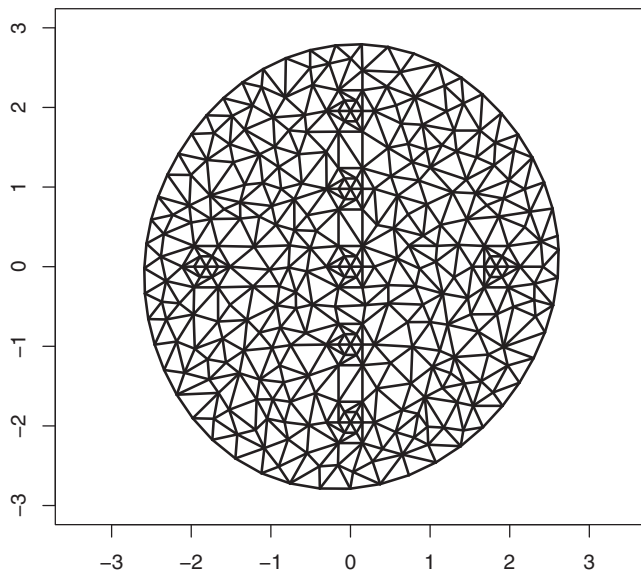
Figure 4. Left: triangulation of the carotid cross-section used in the blood flow velocity field application. Right: illustration of a linear finite element basis function on a triangulation.

4.1.1 Properties of the Estimator. The estimator $\hat{f}_h$ is a linear function of the observed data values. The fitted values $\hat{\mathbf{z}} = \mathbf{\Psi}\hat{\mathbf{f}}$ can be represented as

$$\hat{\mathbf{z}} = \mathbf{S}\mathbf{z} + \mathbf{r},$$

where the smoothing matrix $\mathbf{S} \in \mathbb{R}^{n \times n}$ and the vector $\mathbf{r} \in \mathbb{R}^n$ are obtained as

$$\mathbf{S} = \mathbf{\Psi}\left(\mathbf{\Psi}^T\mathbf{\Psi} + \lambda\mathbf{P}\right)^{-1}\mathbf{\Psi}^T, \quad \mathbf{r} = \mathbf{\Psi}\left(\mathbf{\Psi}^T\mathbf{\Psi} + \lambda\mathbf{P}\right)^{-1}\lambda\mathbf{P}\mathbf{A}^{-1}\mathbf{u},$$

with $\mathbf{P}$ denoting the penalty matrix

$$\mathbf{P} = \mathbf{P}(\mathbf{K}, \mathbf{b}, c) = \mathbf{A}^T\left(\mathbf{R}\right)^{-1}\mathbf{A}. \tag{16}$$

The smoothing matrix $\mathbf{S}$ has the typical form obtained in a penalized regression problem. In particular, the positive definite penalty matrix $\mathbf{P}$ represents the discretization of the penalty term in (2). Notice that, thanks to the variational formulation of the estimation problem, this penalty matrix does not involve the computation of second-order derivatives. Section 3 of the supplementary material available online shows that, in the finite element space used to discretize the problem, $\mathbf{P}$ is in fact equivalent to the penalty matrix $\tilde{\mathbf{P}}$ that would be obtained as direct discretization of the penalty term in (2), and involving the computation of second-order derivatives. Finally, the vector $\mathbf{r}$ is equal to zero when the penalized PDE is homogenous ($u = 0$); notice that when no specific information on the forcing term is available, it is indeed preferable to consider homogenous PDEs.

Thanks to the linearity of the estimator $\hat{\mathbf{z}}$ in the observations, we can easily derive the properties of the estimator and obtain classical inferential tools as pointwise confidence bands and prediction intervals (see also Sangalli, Ramsay, and Ramsay 2013). Let $\mathbf{z}_0 = (f_0(\mathbf{p}_1), \ldots, f_0(\mathbf{p}_n))^T$ be the column vector of evaluations of the true function f_0 at the n data locations. Recalling that in our model definition $\mathbb{E}[\mathbf{z}] = \mathbf{z}_0$ and $\text{cov}(\mathbf{z}) = \sigma^2\mathbf{I}$, we can compute the expected value and the variance of the estimator $\hat{\mathbf{z}}$:

$$\mathbb{E}[\hat{\mathbf{z}}] = \mathbf{S}\mathbf{f}_0 + \mathbf{r} \quad \text{and} \quad \text{cov}(\hat{\mathbf{z}}) = \sigma^2\mathbf{S}\mathbf{S}^T.$$

Since we are dealing with linear estimators, we can use $\text{tr}(\mathbf{S})$ as a measure of the equivalent degrees of freedom for linear estimators (see, e.g., Buja, Hastie, and Tibshirani 1989; Hastie and Tibshirani 1990). Hence, we can estimate σ^2 as

$$\hat{\sigma}^2 = \frac{1}{n - \text{tr}(\mathbf{S})}(\hat{\mathbf{z}} - \mathbf{z})^T(\hat{\mathbf{z}} - \mathbf{z}).$$

The smoothing parameter λ may be selected via generalized cross-validation minimizing the index

$$\text{GCV}(\lambda) = \frac{1}{n\left(1 - \text{tr}(\mathbf{S})/n\right)^2}(\hat{\mathbf{z}} - \mathbf{z})^T(\hat{\mathbf{z}} - \mathbf{z}).$$

4.2 Areal Estimator

Analogously to the case of pointwise observations, also with areal observations we can introduce an equivalent variational formulation of the estimation problem. Specifically, the variational problem associated with (9) can be discretized as

$$\begin{cases} a(\hat{f}_h, \psi_h) - \int_\Omega \hat{g}_h\psi_h = \int_\Omega u\psi_h \\ \lambda a(\varphi_h, \hat{g}_h) + \sum_{i=1}^N \frac{1}{|D_i|}\int_{D_i}\hat{f}_h\int_{D_i}\varphi_h = \sum_{i=1}^N \bar{z}_i\int_{D_i}\varphi_h \end{cases}$$

for all $\psi_h, \varphi_h \in V_{h,0}^r$, where $\hat{f}_h, \hat{g}_h \in V_{h,0}^r$ and $a(\cdot, \cdot)$ is the bilinear form defined in (12).

Let $\bar{\mathbf{z}} = (\bar{z}_1, \ldots, \bar{z}_N)^T$ be the vector of mean values on subdomains $D_1, \ldots, D_N$, and

$$\bar{\mathbf{\Psi}} = \begin{bmatrix} \frac{1}{|D_1|}\int_{D_1}\boldsymbol{\psi}^T \\ \vdots \\ \frac{1}{|D_N|}\int_{D_N}\boldsymbol{\psi}^T \end{bmatrix}$$

be the matrix of spatial means of the basis functions on the subdomains; moreover, introduce the weight matrix $\mathbf{W} = \text{diag}(|D_1|, \ldots, |D_N|)$ (recall that $\bar{\sigma}_i^2 \propto 1/|D_i|$).

The finite element solution $\hat{f}_h$ of the discrete counterpart of the estimation Problem 2 is thus given by $\hat{f}_h = \boldsymbol{\psi}^T\hat{\mathbf{f}}$, where $\hat{\mathbf{f}}$ is

the solution of the linear system

$$\begin{bmatrix} \bar{\boldsymbol{\Psi}}^T \mathbf{W} \bar{\boldsymbol{\Psi}} & \lambda \mathbf{A}^T \\ \mathbf{A} & -\mathbf{R} \end{bmatrix} \begin{bmatrix} \hat{\mathbf{f}} \\ \hat{\mathbf{g}} \end{bmatrix} = \begin{bmatrix} \bar{\boldsymbol{\Psi}}^T \mathbf{W} \bar{\mathbf{z}} \\ \mathbf{u} \end{bmatrix}.$$

Notice that even though the method provides a pointwise surface estimator $\hat{f}_h$, in the areal data framework we are in fact interested in the estimator of the spatial mean of the surface on a subdomain D:

$$\hat{\bar{f}}(D) = \frac{1}{|D|} \int_D \hat{f}.$$

The finite element counterpart of this estimator is defined as

$$\hat{\bar{f}}_h(D) = \frac{1}{|D|} \int_D \hat{f}_h = \bar{\boldsymbol{\psi}}_D^T \hat{\mathbf{f}},$$

where $\bar{\boldsymbol{\psi}}_D = (1/|D| \int_D \psi_1, \ldots, 1/|D| \int_D \psi_{N_{h,0}})^T$.

4.2.1 Properties of the Estimator. The discrete surface estimator $\hat{f}_h$ and the estimator of the spatial average on the subdomains $\hat{\bar{f}}_h$ are linear in the observed data values $\bar{\mathbf{z}}$. The fitted values of the spatial average on the subdomains $D_1, \ldots, D_N$ are defined as $\hat{\bar{\mathbf{z}}} = \bar{\boldsymbol{\Psi}} \hat{\mathbf{f}} = (\hat{\bar{f}}_h(D_1), \ldots, \hat{\bar{f}}_h(D_N))^T$. They can be represented as

$$\hat{\bar{\mathbf{z}}} = \bar{\mathbf{S}} \bar{\mathbf{z}} + \bar{\mathbf{r}},$$

where $\bar{\mathbf{S}} \in \mathbb{R}^{N \times N}$ and $\bar{\mathbf{r}} \in \mathbb{R}^N$ are defined as

$$\bar{\mathbf{S}} = \bar{\boldsymbol{\Psi}} \left(\bar{\boldsymbol{\Psi}}^T \mathbf{W} \bar{\boldsymbol{\Psi}} + \lambda \mathbf{P} \right)^{-1} \bar{\boldsymbol{\Psi}}^T \mathbf{W},$$

$$\mathbf{r} = \bar{\boldsymbol{\Psi}} \left(\bar{\boldsymbol{\Psi}}^T \mathbf{W} \bar{\boldsymbol{\Psi}} + \lambda \mathbf{P} \right)^{-1} \lambda \mathbf{P} \mathbf{A}^{-1} \mathbf{u}.$$

From the definition of model (7) and the linearity of the estimator, we can derive the mean of the estimator

$$\mathbb{E}\left[\hat{\bar{\mathbf{z}}} \right] = \bar{\mathbf{S}} \bar{\mathbf{z}}_0 + \bar{\mathbf{r}}, \tag{17}$$

where $[\bar{\mathbf{z}}_0]_i = 1/|D_i| \int_{D_i} f_0$, and its covariance

$$\text{cov}(\hat{\bar{\mathbf{z}}}) = \bar{\mathbf{S}} \, \text{diag}(\bar{\sigma}_1^2, \ldots, \bar{\sigma}_N^2) \, \bar{\mathbf{S}}^T. \tag{18}$$

It should be noticed that in the areal data framework, the expected value (17) and the variance (18) refer to the estimator of the spatial mean on a subdomain. In fact, even though we can obtain a pointwise estimator for the surface $\hat{f}_h$, we cannot provide an accurate uncertainty quantification for this estimate, because model (7) provides information only on the areal errors η_i. In particular, in the considered areal framework, the variance

$$\text{cov}(\hat{\mathbf{f}}) = \boldsymbol{\Psi} \bar{\boldsymbol{\Psi}}^{-1} \bar{\mathbf{S}} \, \text{diag}(\bar{\sigma}_1^2, \ldots, \bar{\sigma}_N^2) \, \bar{\mathbf{S}}^T \bar{\boldsymbol{\Psi}}^{-T} \boldsymbol{\Psi}^T$$

would underestimate the real variance of $\hat{\mathbf{f}}$.

5. GENERAL BOUNDARY CONDITIONS

All the results presented in Sections 2–4 can be extended to the case of general homogenous and nonhomogenous boundary conditions involving the value of the surface or of its first derivatives at the boundary $\partial \Omega$, allowing for a complex modeling of the phenomenon behavior at the boundary of the domain. The three classic boundary conditions for second-order PDEs are Dirichlet, Neumann, and Robin conditions. The Dirichlet condition controls the value of the function at the boundary, that is, $f|_{\partial \Omega} = \gamma_D$, the Neumann condition concerns the value

of the normal derivative of the function at the boundary, that is, $\mathbf{K} \nabla f \cdot \boldsymbol{v}|_{\partial \Omega} = \gamma_N$, where $\boldsymbol{v}$ is the outward unit normal vector to $\partial \Omega$, while the Robin condition involves the value of a linear combination of first derivative and the value of the function at the boundary, that is, $\mathbf{K} \nabla f \cdot \boldsymbol{v} + \chi f|_{\partial \Omega} = \gamma_R$. We can also impose different boundary conditions on different boundary portions forming a partition of $\partial \Omega$. All the admissible boundary conditions can be summarized as

$$\begin{cases} f = \gamma_D & \text{on } \Gamma_D \\ \mathbf{K} \nabla f \cdot \boldsymbol{v} = \gamma_N & \text{on } \Gamma_N \\ \mathbf{K} \nabla f \cdot \boldsymbol{v} + \chi f = \gamma_R & \text{on } \Gamma_R \end{cases}, \tag{19}$$

where γ_D, γ_N, and γ_R have to satisfy some regularity conditions to obtain a well-defined functional $J(f)$ (see, e.g., Evans 1998).

Under (19), the solution of the estimation problem and of its discrete counterpart also involve boundary terms. Section 2 of the supplementary material available online gives all the details for this general case.

6. SIMULATION STUDIES

In this section, we study the performances of SR-PDE, comparing it to standard SSR and to SOAP in simple simulation studies. We focus on simulation studies that mimic our application setting. The domain Ω is quasi-circular; the true surface f_0, represented in Figure 5, is obtained as a deformation of a parabolic profile using landmark registration and is equal to zero at the boundary of the domain. Likewise for our application, we assume to have a priori information about the shape of the field, that is known to have a quasi-parabolic profile, with almost circular isolines, and to be zero at the boundary.

Since SOAP is not currently devised to deal with areal data, we here consider pointwise observations, with location points sampled on the whole or only on subregions of the domain (Section 4 of the supplementary material available online presents simulation studies comparing SR-PDE with standard SSR in the areal data framework). Specifically, we here consider three cases:

(A) $n = 100$ observation points $\mathbf{p}_1, \ldots, \mathbf{p}_n$ sampled on the entire domain.
(B) $n = 100$ observation points sampled only on the first and third quadrant.
(C) $n = 100$ observation points sampled in a cross-shape pattern.

The experiment is replicated 50 times. For each study case, A, B, and C, and each replicate: we sample the location points, $\mathbf{p}_1, \ldots, \mathbf{p}_n$; we sample independent errors, $\epsilon_1, \ldots, \epsilon_n$, from a Gaussian distribution with mean 0 and standard deviation $\sigma = 0.1$; we thus obtain observations $z_1, \ldots, z_n$ from model (1) with the true function f_0 displayed in Figure 5.

The surface $\hat{f}$ is estimated using three methods:

1. SR-PDE (anisotropic and nonstationary smoothing).
2. Standard SSR (isotropic and stationary smoothing).
3. SOAP (isotropic and stationary smoothing).

For all the three methods, we impose homogenous Dirichlet b.c., $f|_{\partial \Omega} = 0$; for each simulation study, each replicate, and each method, the value of the smoothing parameter λ is chosen via GCV.
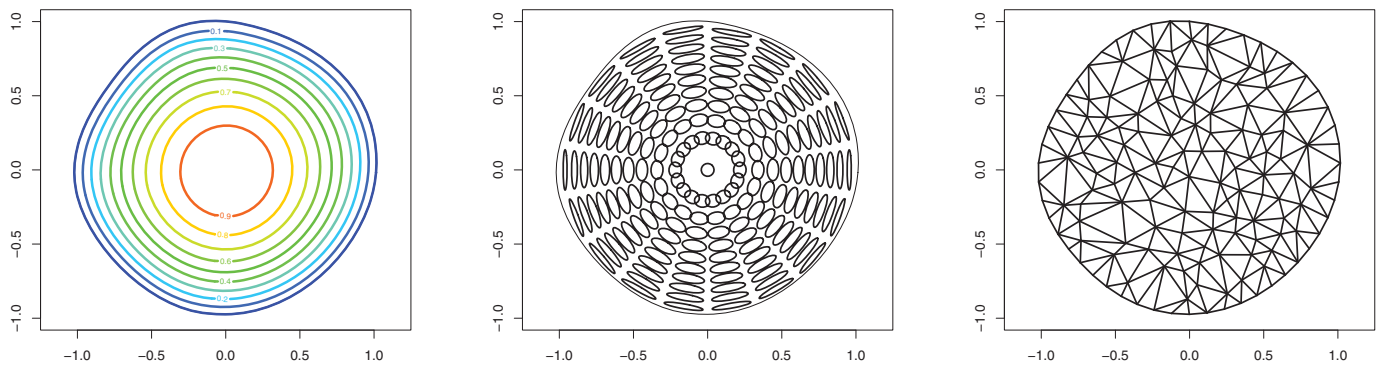
Figure 5. Left: true surface f_0, with almost circular isolines and zero value at the boundary of the domain, used for the simulation studies; the image displays the isolines $(0, 0.1, \ldots, 0.9, 1)$. Center: diffusion tensor field **K** used for SR-PDE. Right: triangulation of the domain used for SSR and SR-PDE.

The triangulation used for the SR-PDE and standard SSR estimation is a uniform mesh on the domain, represented in Figure 5, right, with approximately 100 vertices. Both for SR-PDE and SSR, we use a linear finite element space for the discretization of the surface estimator.

Using SR-PDE, it is possible to incorporate the prior knowledge on the shape of the surface, which should have almost circular isolines. We can achieve this by penalizing a PDE that smooths the surface along concentric circles; specifically we consider the anisotropic and nonstationary diffusion tensor illustrated in the central panel of Figure 5 and given by

$$\mathbf{K}(x, y) = \begin{bmatrix} y^2 + \kappa_1 x^2 & (\kappa_1 - 1)xy \\ (\kappa_1 - 1)xy & x^2 + \kappa_1 y^2 \end{bmatrix} + \kappa_2 \left(R^2 - x^2 - y^2 \right) \mathbf{I}_2, \tag{20}$$

where R denotes the largest radius in this almost circular domain (in the simulations, $R = 1$). The first hyperparameter in (20), κ_1, represents the ratio between the diffusion in the radial and in the circular direction, and we set $\kappa_1 = 0.01$. The anisotropic and nonstationary part of the diffusion field, which corresponds to the first term of the right-hand side of (20), is stronger near the boundary and completely vanishes in the center of the carotid; instead the isotropic and stationary part, which corresponds to the second term of the right-hand side of (20), vanishes near the boundary. The relative strength of the stationary isotropic and nonstationary anisotropic part is controlled via the second hyperparameter κ_2, and we set $\kappa_2 = 0.1$. The transport field, the reaction term, and the forcing term are set equal to zero, that is, $\mathbf{b} = 0$, $c = 0$, and $u = 0$.

Standard SSR instead is not able to take advantage of the specific prior knowledge of the shape of the surface, and enforces an isotropic and stationary smoothing, corresponding to SR-PDE with $\mathbf{K} = \mathbf{I}$, $\mathbf{b} = 0$, $c = 0$, and $u = 0$. Also SOAP produces an isotropic and stationary smoothing; this technique is implemented using the function `gam`, in the R package `mgcv` 1.7–22, see Wood (2011), using 49 interior knots on a lattice.

Figures 6–8 show the results obtained using the different methods in the three considered scenarios, cases A, B, and C. The upper left panel of the figures shows the location points sampled in the first replicate in each of the three different scenarios. The top right, bottom left, bottom right panels of these fig-

ures display the surface estimates obtained using, respectively, SR-PDE, SSR, and SOAP. In particular, the images display the isolines $(0, 0.1, \ldots, 0.9, 1)$ of the surface estimates obtained in the 50 simulation replicates; the isolines are colored using the same color scale used for the isolines of the true function f_0 in Figure 5. These images highlight some aspects of the bias and variance of the surface estimators. The shape of the estimated surfaces emphasizes the main bias aspects of the estimators, while the dispersion or concentration of the isolines highlights, respectively, the larger or smaller variability of the estimator.

Comparing the results obtained with the three methods we can notice that the inclusion of the prior knowledge improves the estimate, especially when data are distributed only on subregions of the domain. We can in fact see that in the three case studies the surfaces estimated with SR-PDE smoothing have circular isolines similar to those of the true surface f_0. Instead, when the prior knowledge is not included in the model, that is, for standard SSR and SOAP, the surface estimates tend to depend on the design of the experiments. We notice in fact that the isolines of SSR and SOAP estimates are similar to ellipses in case B and to rhomboids in case C, instead of circles. This is because both methods tend to fit planes in those areas where no observations are available. This phenomenon is more apparent with SSR than with SOAP because SOAP estimates have an higher variability.

Figure 9 shows the comparison of the three methods in terms of root mean square error (RMSE) of the corresponding estimators, with the RMSE evaluated on a fine lattice of step 0.01 over the domain Ω. The boxplots highlight that the incorporation of the prior knowledge on the shape of the surface leads to a large improvement in the estimation. SR-PDE smoothing provides in fact significantly better estimates of f_0 than the other two methods. The boxplots also show that SR-PDE estimates display lower variability than SSR and SOAP estimates. This phenomenon is also visible from the isolines of the estimated surfaces with SR-PDE, SSR, and SOAP represented in Figures 6–8.

The simulation studies reported in Section 4 of the supplementary material available online show that incorporating the prior knowledge on the phenomenon leads to significantly improved estimates also in the areal data framework.
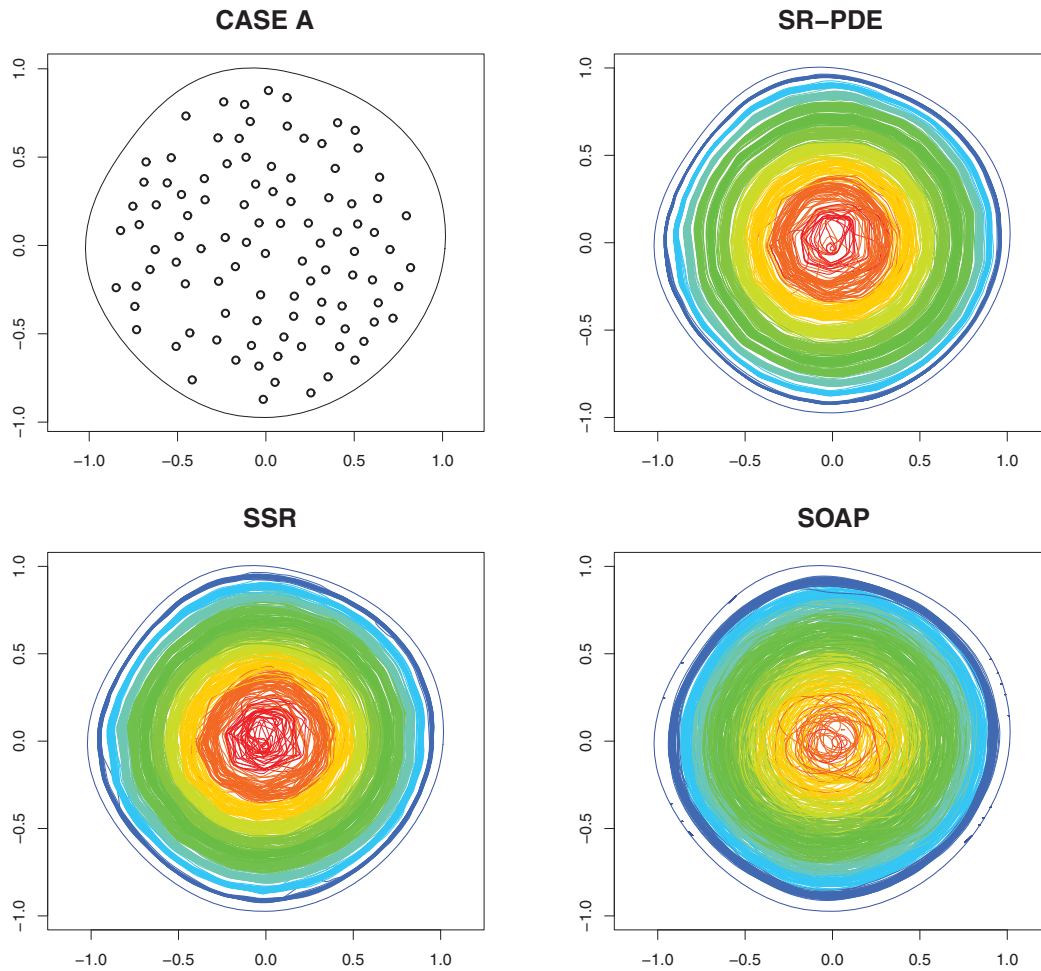
Figure 6. Top left: location points sampled in the first replicate for case A. Top right, bottom left, bottom right: surface estimates obtained using, respectively, SR-PDE, SSR, and SOAP; the images display the isolines $(0, 0.1, \ldots, 0.9, 1)$ of the surface estimates obtained in the 50 simulation replicates; the isolines are colored using the same color scale used for the isolines of the true function f_0 in Figure 5.

7. APPLICATION TO THE BLOOD FLOW VELOCITY FIELD ESTIMATION

Carotid ECD is usually the first imaging procedure used to diagnose carotid artery diseases, such as ischemic stroke, caused by the presence of an atherosclerotic plaque. ECD data in our study have been collected using a Diagnostic Ultrasound System Philips iU22 (Philips Ultrasound, Bothell, U.S.A.) with a L12-5 probe. The septum that divides the carotid bifurcation is localized and marked as a reference point. With the help of an electronic rule, we localize the other points of acquisition of the blood velocity; specifically, in our protocol the blood flow velocity is measured in standard locations points, according to the cross-shaped design represented in Figure 1, right panel, on the carotid cross-section located 2 cm before the reference point indicated above.

To estimate the systolic velocity field on this cross-section of the carotid, we minimize the functional $\bar{J}(f)$ defined in (8). As mentioned in Section 1, we know that a physiological velocity profile has smooth and almost circular isolines. For this reason, we choose to penalize a PDE that includes the nonstationary anisotropic diffusion tensor shown in the left panel of Figure 3 and described in Equation (20), that smooths the observations in the tangential direction of concentric circles. The largest section

radius is $R = 2.8$; we set $\kappa_1 = 0.1$, to impose a smoothing effect that is one order of magnitude stronger in the tangential direction of circles than in the radial direction, and $\kappa_2 = 0.2$, to impose an amount of isotropic smoothing in the center of the vessel that is comparable to the anisotropic smoothing in the periphery of the vessel. Moreover, we also know that, due to viscosity of the blood, a physiological velocity field is rather flat on the central part of the artery lumen. For this reason, we also include in the PDE model the nonstationary transport field shown in the right panel of Figure 3, which smooths the observations in the radial direction, from the center of the cross-section to the boundary: $\mathbf{b}(x, y) = (\beta x, \beta y)^T$, where the hyperparameter β represents the intensity of the transport field. This transport term in fact penalizes high first derivatives in the radial direction, providing velocity profiles that tend to flatten in the central part of the artery lumen. Here, we set $\beta = 0.5$ to impose a smoothing effect that is comparable to the anisotropic smoothing induced by the diffusion term. The reaction parameter and the forcing term are not needed in this application, hence we set $c = 0$ and $u = 0$. Finally, we know that blood flow velocity is zero at the arterial wall, due to friction between the blood particles and the vessel wall (the above-mentioned no-slip conditions); hence we impose homogenous Dirichlet b.c.: $f|_{\partial\Omega} = 0$. The problem is
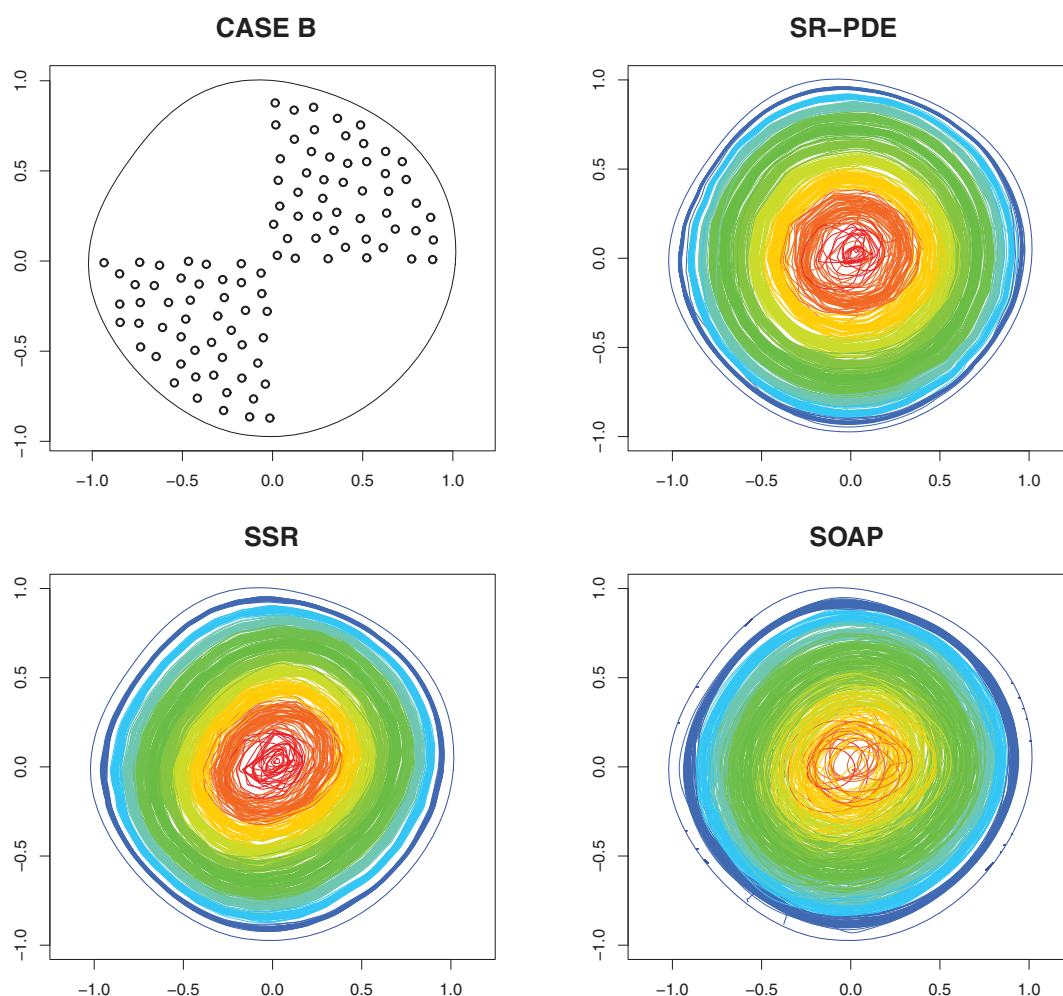
CASE B

SR–PDE

SSR

SOAP

Figure 7. Same as Figure 6, for case B.

then discretized by means of linear finite elements defined on the mesh represented in Figure 4, left panel.

Figure 10 displays the velocity field estimated using SR-PDE smoothing. The maximum estimated velocity is 31.75 cm/sec with an estimated standard deviation $\hat{\sigma} = 1.92$ cm/sec. A visual comparison with the estimate obtained for the same data by standard SSR, shown in Figure 2, immediately highlights the advantages of the proposed technique. While the standard SSR estimate is strongly influenced by the cross-shaped pattern of the observations and displays strongly rhomboidal isolines, forcing the surface estimate toward a plane in regions where no observations are available, the SR-PDE efficiently uses the a priori information on the phenomenon under study and returns a realistic estimate of the blood flow, which is not affected by the cross-shaped pattern of the observations and displays physiological and smooth isolines.

Notice that the SR-PDE estimate in Figure 10 captures an asymmetry in the data, resulting in an eccentric estimate of the blood flow: the velocity peak is in fact not in the center of the cross-section but in the lower part where higher velocities are measured. This feature of the blood flow is indeed justified by the curvature of the carotid artery and by the nonstationarity of the blood flow. SR-PDE estimates in fact accurately highlight important features of the blood flow, such as eccentricity,

asymmetry, and reversion of the fluxes, that are of interest to the medical doctors, to understand how the local hemodynamics influences atherosclerosis pathogenesis. As mentioned in the Introduction, MACAREN@MOX project aims at exploring this relationship, investigating how different hemodynamical patterns affect the plaque formation process. For this reason, obtaining accurate physiological estimates of blood flow velocity fields is a first crucial goal of the project. Indeed, the SR-PDE estimates will then be used in population studies that compare the blood flow velocity field in patients versus healthy subjects, and that compare the velocity field in patients before and after the removal of the carotid plaque via thromboendarterectomy.

Notice that such population studies involve the comparisons of estimates referred to different domains, since the cross-sections of the carotids have patient-specific shapes; to face this issue we are currently developing an appropriate registration method (see Section 8) and these analyses will be the object of a following dedicated work. The estimated velocity fields will also be used as inflow conditions for the hemodynamic simulations performed using patient-specific carotid morphologies. The prescription of suitable inflow conditions in computational fluid-dynamics is in fact a major issue; see, for example, Veneziani and Vergara (2005). Moreover, the computation of the variance of the surface estimator will also be used
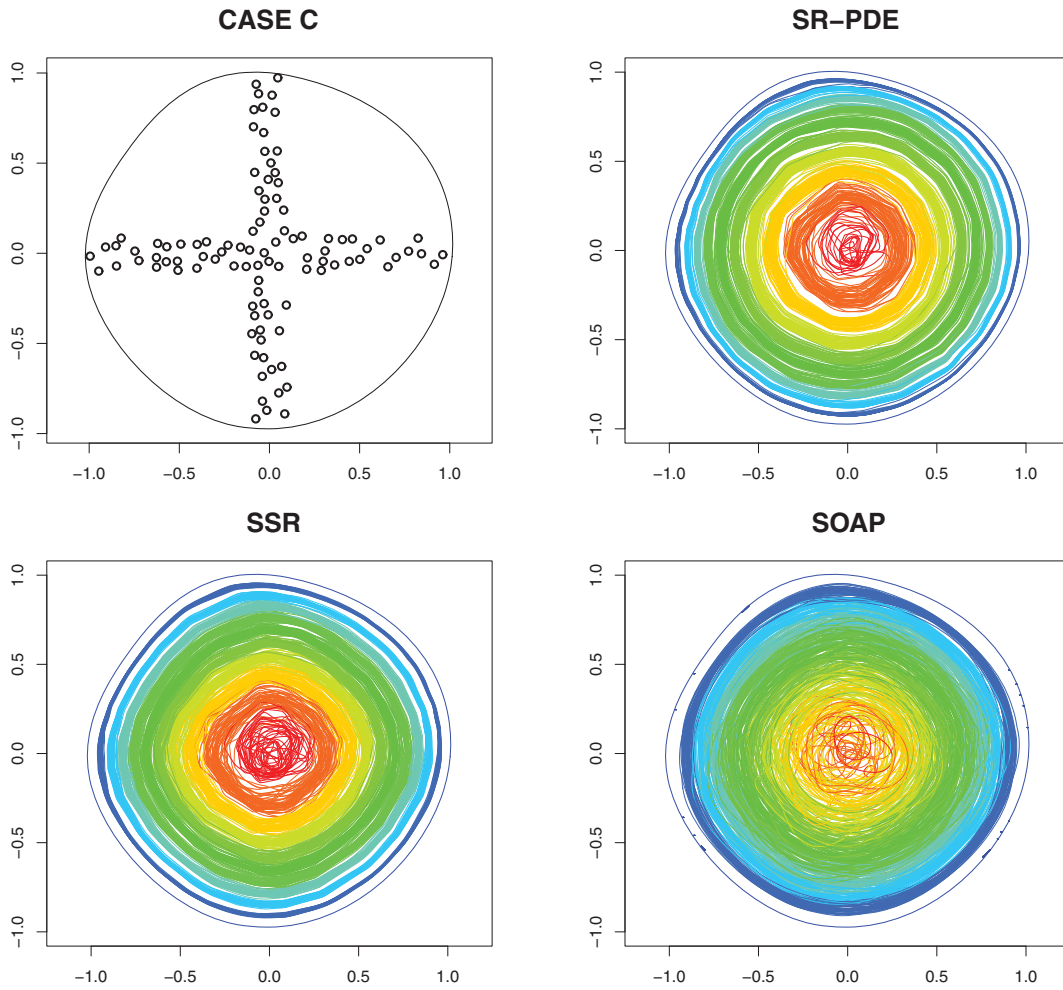
Figure 8. Same as Figure 6, for case C.

to investigate the sensitivity of these simulations to the specified inflow conditions and will provide some understanding on how their misspecification affects the results. These numerical simulations will in turn offer enhanced data that give a richer information on hemodynamical regimes in the carotid bifurcation, further allowing the study of its impact on atherosclerosis. Computational fluid-dynamic simulations are also of great interest because they allow to synthetically verify the impact of different surgical interventions, evaluating which one is more prone to the reformation of the plaque or to other complications. In the future, this could become an important tool for comparing beforehand the effects of different interventions for a given patient, considering the geometry of the patient carotid and the properties of the atherosclerotic plaque, thus giving important suggestions to clinicians on the surgical operation to choose in the specific patient case.
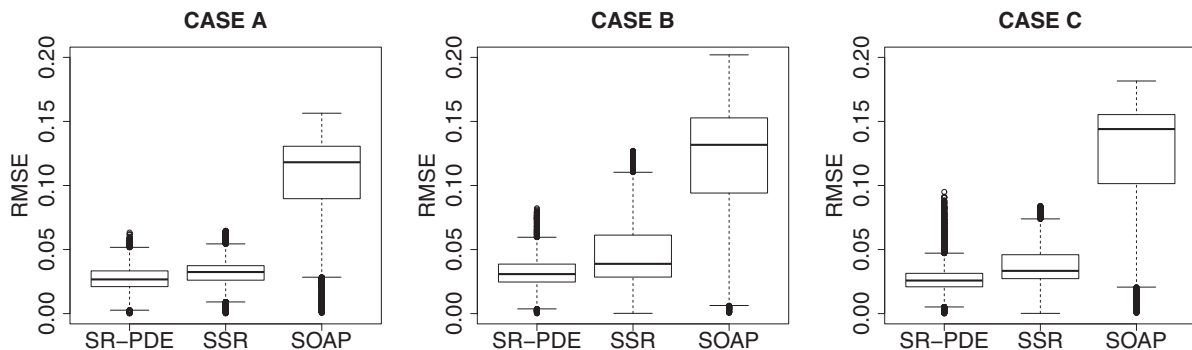
Figure 9. Boxplot of RMSE (evaluated on a fine lattice of step 0.01 over the domain Ω) for SR-PDE, SSR, and SOAP estimators, in case studies A, B, and C.
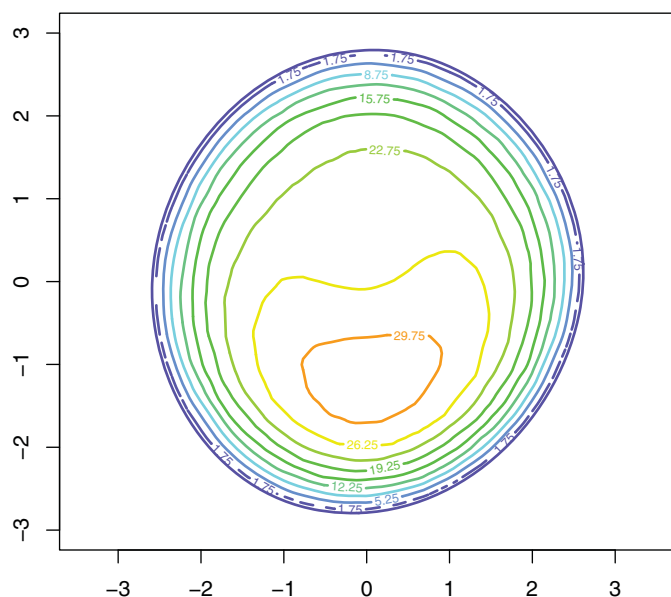
Figure 10. Estimate of the blood flow velocity field in the carotid section using SR-PDE.

8. CONCLUSION AND FUTURE WORK

In this work, we have introduced an innovative method for surface and spatial field estimation, when prior knowledge is available, concerning the physics of the problem. In particular, this prior knowledge, conveniently described via a PDE, is used to model the space variation of the phenomenon. Although demonstrated on the specific application that motivated its development, the method has indeed a very broad applicability, since PDEs are commonly used to model phenomena behavior in many fields of sciences and engineering.

One of the most interesting developments within this line of research consists now in the data-driven estimation of the hyperparameters in the penalized PDE. In the current study, these hyperparameters have in fact been considered fixed. Notice that, while a currently crucial topic in statistics concerns the development of methods for parameter estimations in ordinary differential equation, this would instead consist in approaching the remarkably more complex problem of data-driven estimation of the parameters in PDEs. Although this research field is subject of specific interest by the inverse problem community (see, e.g., Stuart 2010), we believe that statisticians have not yet devoted much attention to this problem. Within the considered framework, a possible road to tackle this problem is offered for instance by the parameter cascading methodology proposed in Ramsay et al. (2007). A first promising attempt to apply this methodology to the parameter estimation in PDEs is provided in Xun et al. (2013).

As derived in Section 4, the proposed estimators are linear in the observed data values and have a typical penalized regression form, so that important distributional properties can be readily derived. We are currently also studying the (infill) asymptotic properties of these estimators, when the number of observations n goes to infinity and the characteristic mesh size h goes to zero. The numerical convergence of the estimator when h goes to zero is detailed in Azzimonti et al. (2014).

The proposed method can also be extended to include the time dimension, to model surfaces evolving in time. Such extension would allow to study how the blood flow velocity field varies during the time of the heart-beat. Notice that it is necessary in this case to allow for changes of the shape of the domain over time, to account for the deformation of the artery wall during the heartbeat. This poses a problem of registration of different domains similar to the one faced in population studies (see Section 7).

Finally, the method could also be extended to Riemannian manifold domains, by appropriately setting the problem in the framework presented in Ettinger, Perotto, and Sangalli (2012).

SUPPLEMENTARY MATERIALS

The supplementary material available online is organized as follows. Section 1 gives the Proof of Propositions 1 and 2 and details the regularity conditions required for Problems 1 and 2. Section 2 deals with the case of more general boundary conditions. Section 3 discusses the penalization matrix. Finally, Section 4 reports some simulation studies with areal data.

[Received June 2013. Revised June 2014.]

REFERENCES

Azzimonti, L., Nobile, F., Sangalli, L., and Secchi, P. (2014), "Mixed Finite Elements for Spatial Regression With PDE Penalization," *SIAM-ASA Journal on Uncertainty Quantification*, 2, 305–355. [1070]

Buja, A., Hastie, T., and Tibshirani, R. (1989), "Linear Smoothers and Additive Models," *The Annals of Statistics*, 17, 153–555. [1064]

D'Elia, M., Perego, M., and Veneziani, A. (2012), "A Variational Data Assimilation Procedure for the Incompressible Navier-Stokes Equations in Hemodynamics," *Journal of Scientific Computing*, 52, 340–359. [1057]

D'Elia, M., and Veneziani, A. (2012), "Uncertainty Quantification for Data Assimilation in a Steady Incompressible Navier-Stokes Problem," *ESAIM Mathematical Modelling and Numerical Analysis*, 47, 1037–1057. [1057]

Ettinger, B., Perotto, S., and Sangalli, L. (2012), "Spatial Regression Models Over Two-dimensional Manifolds," Technical Report 54/2012, MOX - Dipartimento di Matematica, Politecnico di Milano. Available at *http://mox.polimi.it/it/progetti/pubblicazioni/*. [1070]

Evans, L. (1998), *Partial Differential Equations*, Providence, RI: American Mathematical Society. [1059,1065]

Formaggia, L., Quarteroni, A., and Veneziani, A. (2009), *Cardiovascular Mathematics: Modeling and Simulation of the Circulatory System*, Milano: Springer. [1059]

Guillas, S., and Lai, M. (2010), "Bivariate Splines for Spatial Functional Regression Models," *Journal of Nonparametric Statistics*, 22, 477–497. [1059]

Hastie, T., and Tibshirani, R. (1990), *Generalized Additive Models*, London: Chapman and Hall Ltd. [1064]

Hinze, M., Pinnau, R., Ulbrich, M., and Ulbrich, S. (2009), *Optimization With PDE Constraints*, Berlin: Springer. [1059]

Lindgren, F., Rue, H., and Lindström, J. (2011), "An Explicit Link Between Gaussian Fields and Gaussian Markov Random Fields: The Stochastic Partial Differential Equation Approach," *Journal of the Royal Statistical Society*, Series B, 73, 423–498. [1059]

Lions, J. (1971), *Optimal Control of Systems Governed By Partial Differential Equations*, Berlin: Springer. [1059]

Moyle, K., Antiga, L., and Steinman, D. (2006), "Inlet Conditions for Image-based CFD Models of the Carotid Bifurcation: Is it Reasonable to Assume Fully Developed Flow?," *Journal of Biomechanical Engineering*, 128, 371–379. [1057]

Pironneau, O., Hecht, F., Le Hyaric, A., and Morice, J. (2011), *FreeFem++ Software version 3.16*, available at *www.freefem.org*. [1059]

Quarteroni, A. (2008), *Numerical Models for Differential Problems*, Milano: Springer. [1059,1061,1062]

Ramsay, T. (2002), "Spline Smoothing over Difficult Regions," *Journal of the Royal Statistical Society*, Series B, 64, 307–319. [1058,1059,1060]

Ramsay, J., Hooker, G., Campbell, D., and Cao, J. (2007), "Parameter Estimation for Differential Equations: A Generalized Smoothing Approach," *Journal of the Royal Statistical Society,* Series B, 69, 741–796. [1070]

R Development Core Team (2012), *R: A Language and Environment for Statistical Computing*, Vienna: R Foundation for Statistical Computing, available at *www.R-project.org*. [1059]

Rozza, G., Manzoni, A., and Negri, F. (2012), "Reduction Strategies for PDE-constrained Optimization Problems in Haemodynamics," in *Proceedings of ECCOMAS 2012, European Congress on Computational Methods in Applied Sciences and Engineering.* [1057]

Sangalli, L., Ramsay, J., and Ramsay, T. (2013), "Spatial Spline Regression Models," *Journal of the Royal Statistical Society,* Series B, 75, 681–703. [1058,1059,1060,1061,1064]

Stuart, A. (2010), "Inverse Problems: A Bayesian Perspective," *Acta Numerica*, 19, 451–559. [1059,1060,1070]

Veneziani, A., and Vergara, C. (2005), "Flow Rate Defective Boundary Conditions in Haemodynamics Simulations," *International Journal for Numerical Methods in Fluids*, 47, 803–816. [1068]

Wood, S. (2011), "Fast Stable Restricted Maximum Likelihood and Marginal Likelihood Estimation of Semiparametric Generalized Linear Models," *Journal of the Royal Statistical Society,* Series B, 73, 3–36. [1066]

Wood, S., Bravington, M., and Hedley, S. (2008), "Soap Film Smoothing," *Journal of the Royal Statistical Society,* Series B, 70, 931–955. [1058]

Xun, X., Cao, J., Mallick, B., Maity, A., and Carroll, R. (2013), "Parameter Estimation of Partial Differential Equation Models," *Journal of the American Statistical Association*, 108, 1009–1020. [1070]